Energy and exergy analysis of a glazed solar preheating collector wall with non-uniform perforated corrugated plate

Gao, Meng; Fan, Jianhua; Furbo, Simon; Xiang, Yutong

Published in:
Renewable Energy

Link to article, DOI:
10.1016/j.renene.2022.07.026

Publication date:
2022

Document Version
Publisher's PDF, also known as Version of record

Renewable Energy 196 (2022) 1048–1063

Contents lists available at ScienceDirect

Renewable Energy

journal homepage: www.elsevier.com/locate/renene

Energy and exergy analysis of a glazed solar preheating collector wall with non-uniform perforated corrugated plate

Meng Gao, Jianhua Fan*, Simon Furbo, Yutong Xiang

DTU Civil Engineering, Technical University of Denmark, Brovej 118, 2800 Kgs, Lyngby, Denmark

ARTICLE INFO

Article history:
Received 6 February 2022
Received in revised form
13 June 2022
Accepted 4 July 2022
Available online 15 July 2022

Keywords:
Glazed solar preheating collector wall
Exergy analysis
Numerical simulation
Non-uniform perforated corrugated plate

ABSTRACT

The solar preheating wall provides an effective solution to the conflict between the requirement for fresh air and the need for heat conservation in winter by preheating fresh ventilation air. In this paper, a study of the glazed solar preheating collector wall is carried out by numerical simulation with the aim of improving heat collection efficiency through structural optimization. The influence of the environment as well as its range of applications are investigated. The characteristics of the internal flow and temperature distribution are obtained to facilitate the structural analysis. The influence of air volume and structural parameters on thermal efficiency is investigated, providing a good reference for structural design optimization. In addition, it is observed that the exergy efficiency of the optimized design is 1.3 times higher than that of the conventional solar wall, while the thermal efficiency is 15% higher than traditional ones. The heat loss rate is reduced by 40% in high wind and extremely cold regions compared to that of the unglazed one. The maximum supply percentage can reach 69.4% and the temperature rise is approximately 20 °C. Finally, a parametric investigation is carried out on different functional buildings, and an optimal structure in Xi'an is given as a reference. The energy collection and transfer efficiency increase with the increase of air volume, but the energy saving rate decreases. The results indicate that this solar wall is ideal for buildings with low fresh air demand, such as single residences and small offices. It also has a considerable preheating effect on high fresh air demand ones.

1. Introduction

Building energy efficiency and renewable energy utilization are the two main ways to reduce conventional energy consumption in buildings. Relying on renewable energy sources for building energy supply becomes an almost necessary option [1]. Solar energy becomes the primary choice for clean energy utilization compared to other energy sources that are limited in terms of geography, extraction conditions and total amount of energy [1,2].

1.1. Solar preheating wall

Passive solar architecture can provide a significant portion of the heating energy for the rooms using solar energy [2]. Currently, with the emphasis on disease prevention and efficiency, there is an increasing demand for air quality [3]. The huge additional heat load from fresh air in winter brings a challenge for energy saving: how to create comfortable living conditions for both thermal environment and air quality? The original heat-collecting walls were modified to add active fresh air introduction and then solar preheating wall was created [4].

The solar preheating wall usually consists of a glass cover, a black porous metal plate, a flow channel, an suction fan, and an adiabatic shell [5]. Installed on the south wall, it can provide larger heat collection area. In addition, the removable structure allows the collector wall to be installed easily and quickly. It also beautifies the appearance of the building and increases thermal storage of the facade.

1.2. Glazed transpired solar collector wall

The Glazed Transpired Collector (GTC) has gained a lot of interest. Many researchers have studied them in order to optimize their structure for efficiency.

For the purpose of heat transfer process analysis and theoretical modeling, a time-dependent heat transfer model was developed by Bansal et al. [6] to predict the daily performance of a conventional

* Corresponding author.
E-mail address: jifa@dtu.dk (J. Fan).

https://doi.org/10.1016/j.renene.2022.07.026

solar air heater. It was found that the effective heat transfer coefficient from the absorber plate to the air stream has a significant effect on the daily response of the solar air heater. Li et al. [7,8] developed a mathematical model for predicting the thermal performance of solar collectors based on the energy balance equation. The average deviation of the experimental results from the simulated results was 2.25%. El-sebaii et al. [9] conducted a theoretical and experimental study on dual-channel v-shaped corrugated solar air heater. The results showed that the efficiency of the two-channel v-shaped corrugated solar air heater was 9.3%–11.9% higher than the finned one.

In terms of structural and material optimization and efficiency improvement purposes, Choudhury et al. [10] evaluated the effect of fixed pressure drop and specific air mass flow rate in solar air heaters of different shapes and found ways to improve the efficiency of the system with minimum cost. Roozbeh et al. [11] evaluated different colors of porous glass solar air heaters (PGSAH): Black non glass permeable solar air heaters (UTSAH) were experimentally investigated for their thermal performance. Zheng et al. [12,13] investigated a new type of corrugated metal-filled solar collector. The results showed that the corrugated metal solar collector has higher heat transfer coefficient. Li et al. [14] found that the height of the collector and the solar transmission rate of the vacuum glass cover significantly affect the heat collection efficiency. Ho et al. [15] investigated experimentally a device for inserting an absorber plate into a double-pass channel of a recirculating flat-plate solar air heater. Brij et al. [16] investigated the size of the artificial roughness on the performance of solar wall. The thermal and effective efficiency of the rough solar wall was significantly improved compared to the smooth one.

In the aim of practical application effect and improvement, a GTC-based solar wall system was proposed as a solution by Zhang et al. [17]. The indoor air temperature distribution and the changes of CO, CO2, PM2.5 and PM 10 concentrations were simulated numerically. Eryener et al. [18] studied a new solar updraft wall and monitored solar radiation in summer and winter. The results showed that the heat collection efficiency of the solar collector wall ranged from 60%–80%. Gao et al. [19] found that despite optical losses, glass can be used to reduce convective losses caused by high lateral wind speeds. This provides economy and high thermal efficiency in cold rural areas.

According to numerous studies, it has been found that the suction effect of the holes not only increases the convective heat transfer, but also significantly reduces the surface heat loss [20]. Therefore removing the glass cover can result in a higher heat collection rate. A new branch of solar fresh air preheat wall research, the unglazed transparent collector (UTC), emerged [21].

1.3. Unglazed transpired solar collector wall

UTC was proposed in the early 1990s as a product of a private solar heating and energy efficiency company and the National Renewable Energy Laboratory (NREL) [22]. Njomo et al. [23] analyzed the heat transfer of UTC using a mathematical model and investigated the effects of parameters on the heat performance of the absorber plate. Shukla et al. [24] discussed and compared various UTC models and showed that the most critical factors affecting the efficiency of UTC are wind speed, flow rate, porosity and absorption rate. Croitoru et al. [25] analyzed the effect of permeation pore shape on heat transfer. It was found that the flow of a lobed infiltration penetration is more complex and has better heat transfer performance than a circular infiltration penetration. Li et al. [26,27] proposed an energy model for UTC and the energy model was validated in an outdoor test facility. The root mean square error (RMSE) of the UTC model was within 1 °C. Motahar et al. [28] used a steady-state model to calculate the heat transfer and pressure drop in the perforated plate and back wall. Golneshan et al. [29] analyzed the exergy performance of the UTC and optimized the geometry, pore spacing, and pore diameter of the UTC. Chan et al. [30] compared the heat collection efficiency of flat plate with black aluminum plate and concluded that the heat collection efficiency of the black plate was higher than that of the flat plate.

In view of improving the practical application effect, Esmaeel et al. [31] combined a glass-free permeable solar collector with an air-source heat pump. The results show that the combination of a 2.5 kW/m^2 heat pump with a 2.5 m^2 solar collector can reduce the electricity consumption of the heat pump by 10%. Leon et al. [32] developed a mathematical model of UTC to predict the effect of porosity, airflow rate and solar absorption/thermal radiation rate on UTC mesothermal performance. The results show that the thermal efficiency of the UTC is good at 45–55 °C and can be used as a heating device of the drying chamber.

1.4. Existing problems and research purposes

However, the aforementioned studies do not address the essential limitations of UTC. For instance, the large temperature difference between the heat collection wall surface and the ambient in extremely cold regions causes back-flow heat loss. In regions with large side winds, the boundary layer suction is broken and the outward sweeping side winds will cause significant heat losses. In recent years, with the advancement of glass materials and the expansion of renewable energy demand [33], GTC has been brought back to the application. It has a translucent cover, which leads to a reduction in short-wave radiation heat absorption but also a significant reduction in ambient convection and long-wave radiation heat loss. Therefore, GTC is advantageous in the above-mentioned extreme areas. The biggest problem is that its energy collection rate and heat exchange rate need to be improved urgently. Previous investigations of GTC have been limited to increasing roughness and surface area of the collector plate, and less research has been done to increase convective heat transfer using GTC double channels and near-wall vortex.

Based on this, a glazed solar preheating collector wall with non-uniformly perforated corrugated plate (GSPW) is proposed to solve this problem. It has the advantage of increasing visible light transmission using acrylic and increasing convective heat transfer by adding corrugated heat transfer surfaces and double channels secondary heat transfer.

In this paper, the variation characteristics of flow and heat transfer in GSPW due to the structure and ventilation mode are systematically studied. The influence laws of different key design parameters on exergy efficiency as well as thermal efficiency are also investigated. Finally, the scope of suitability of GSPW in different buildings is studies.

2. Description of GSPW

2.1. Structure and heat transfer

The glazed solar preheating collector wall (GSPW) is composed of a light-weight black V-shaped corrugated aluminum plate with small round holes, an acrylic plate with a transmittance rate exceeding 90%, a fresh air inlet and a thermal insulation shell, as shown in Fig. 1. In order to increase the temperature rise, the thickness of the aluminum plate is less than 1 mm. The acrylic plate has a square opening at the bottom for fresh air intake and drainage.

In winter, the outdoor cold air enters the channel-1 between the acrylic plate and the solar absorber plate through the fresh air inlet.

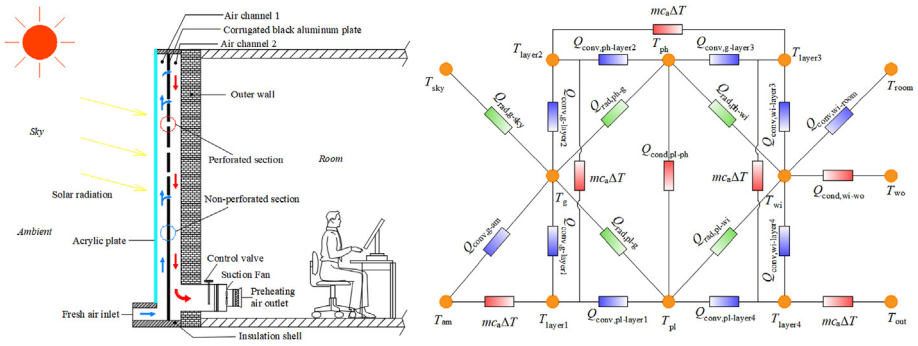

Fig. 1. Structure and heat transfer network of GSPW.

The heat transfer network is demonstrated in Fig. 1. Subsequently, the fresh air conducts the first heat exchange with corrugated plate, the heat transfer zone called layer-1. The secondary heat exchange with the corrugated penetration plate conducts in layer-2 due to hole suction force. The hole jet impinges into the channel-2 between the outer wall and the solar absorber plate, which conducts the third heat exchange with the back of corrugated penetration plate in layer-3. The function of the suction fan is to guide the air flow downward and conduct the fourth heat exchange with the back of the corrugated plate in layer-4. The preheated air with sufficient heat exchange is sent into the room through the outlet to improve the indoor temperature and air quality.

2.2. Flow characteristics in channel

Previous researchers have done a huge amount of works on flat plate flow and heat transfer. However, there are large differences in the flow characteristics of corrugated plates and flat plates according to Leonardo [34]. Fig. 2 (a) and (b) illustrate the boundary layer variation of non-perforated and perforated corrugated plate, respectively. The boundary layer of non-perforated corrugated plate section is continuous and progressive due to the large thickness of the boundary layer. In general, vortex will be generated between the wave valleys but no fluid separation will occur. Therefore, there will be transition points to take over the flow connection between the wave peak and the wave valley. The front and back of the absorber plate do not interfere with each other so the flow conditions are consistent.

In contrast, the boundary layer of the perforated plate section is peeled off at holes. The thickness of the boundary layer is also thinner due to the suction effect of the small holes. In addition, the presence of corrugation disturbs the continuity of the boundary layer. The channels at double face of the absorber plate are connected by holes therefore the front and back flows interfere with each other resulting in large differences. Thus, it is possible to generate more than one vortex currents at the peaks and valleys of the waves while completely changing the initial heat transfer properties. This needs to be further validated by simulations for the situations.

3. Methodology

In this paper, the internal flow, heat transfer effect, and energy consumption of GSPW are comprehensively studied by CFD simulation.

3.1. Thermal equilibrium analysis

As shown on the right side of Fig. 1, five heat balances exist in the direction from the inlet (T_{am}) to the outlet (T_{out}), namely: the heat

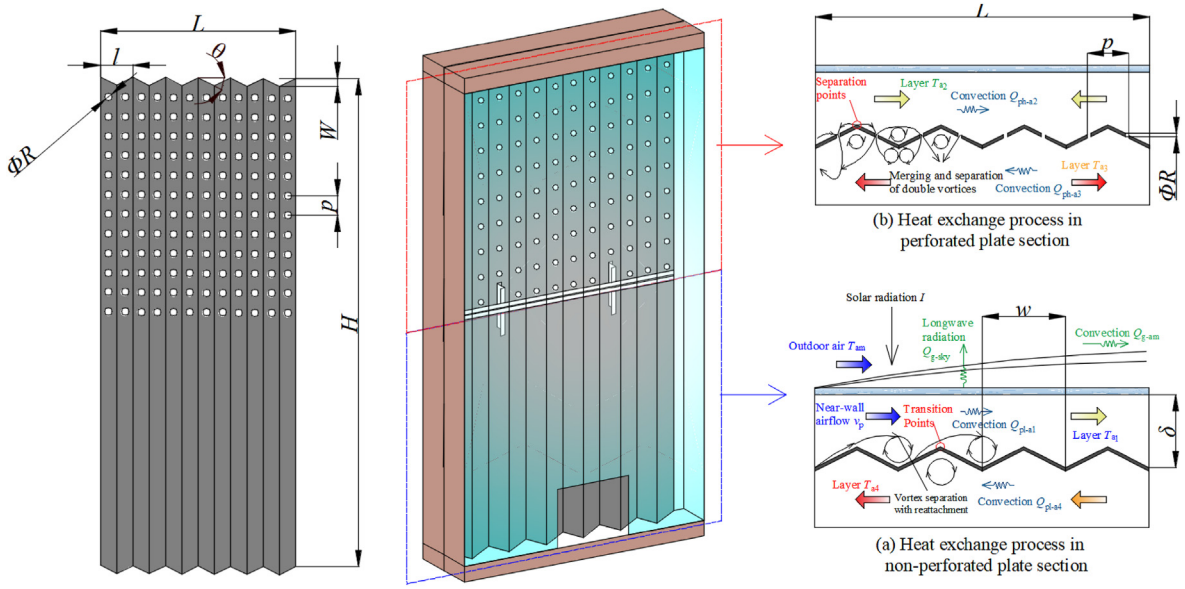

Fig. 2. Schematic diagram and flow characteristic of the GSPW.

balance equations for the glass, channel-1, the heat absorber plate, the channel-2 and the wall. Among them, the surface of the heat absorber plate is subdivided into perforated plate and non-perforated plate. The channel-1 is subdivided into layer-1 and layer-2. The channel-2 is subdivided into layer-3 and layer-4.

Thermal equilibrium equation of the non-perforated plate can be expressed as:

$$Ia_p\beta_g A_{pl} - C_p M_{pl}\frac{\partial T_{pl}}{\partial \tau} = Q_{conv,pl-layer1} + Q_{conv,pl-layer4} + Q_{rad,pl-wi} + Q_{rad,pl-g} + Q_{cond,pl-ph} \quad (1)$$

where, I is solar irradiation, α_p is absorbance of the solar absorber plate, β_g is the glass transmittance, A_{pl} is the non-perforated plate area, C_p is the specific heat capacity of plate, M_{pl} is the weight of the non-perforated plate, T_{pl} is the temperature of the non-perforated plate.

Thermal equilibrium equation of the perforated plate can be expressed as:

$$Ia_p\beta_g A_{ph} - C_p M_{ph}\frac{\partial T_{ph}}{\partial \tau} = Q_{conv,ph-layer2} + Q_{conv,ph-layer3} + Q_{rad,ph-wi} + Q_{rad,ph-g} - Q_{cond,pl-ph} \quad (2)$$

where, A_{ph} is the perforated plate area, M_{ph} is the weight of the perforated plate, T_{ph} is the temperature of the perforated plate.

Thermal equilibrium equation of the glass can be expressed as:

$$IA_g a_g - C_g M_g\frac{\partial T_g}{\partial \tau} = Q_{conv,g-am} + Q_{rad,g-sky} + Q_{rad,g-gound} + Q_{conv,g-layer1} + Q_{conv,g-layer2} - Q_{rad,ph-g} - Q_{rad,pl-g} \quad (3)$$

where, α_g is absorbance of the glass, A_g is the glass, C_g is the specific heat capacity of glass, M_g is the weight of the glass, T_g is the temperature of the glass.

Thermal equilibrium equations of the wall can be expressed as:

$$C_w M_w\frac{\partial T_w}{\partial \tau} = Q_{cond,wi-wo} + Q_{conv,wo-room} + Q_{conv,wi-layer3} + Q_{conv,wi-layer4} - Q_{rad,ph-wi} - Q_{rad,pl-wi} \quad (4)$$

where, C_w is the specific heat capacity of wall, M_w is the weight of the wall, T_w is the temperature of the wall.

Thermal equilibrium equations of the layer-1 to the layer-4 can be expressed as:

$$mc_p\left[T_{layer1} - T_{am}\right] + mc_p\left[T_{layer1} - T_{layer2}\right] = Q_{conv,pl-layer1} + Q_{conv,g-layer1} \quad (5)$$

$$mc_p\left[T_{layer2} - T_{layer3}\right] - mc_p\left[T_{layer1} - T_{layer2}\right] = Q_{conv,ph-layer2} + Q_{conv,g-layer2} \quad (6)$$

$$mc_p\left[T_{layer3} - T_{layer4}\right] - mc_p\left[T_{layer2} - T_{layer3}\right] = Q_{conv,ph-layer3} + Q_{conv,wi-layer3} \quad (7)$$

$$mc_p\left[T_{layer4} - T_{out}\right] - mc_p\left[T_{layer3} - T_{layer4}\right] = Q_{conv,pl-layer4} + Q_{conv,wi-layer4} \quad (8)$$

where, c_p is the specific heat capacity of air, m is the quality of air, T_{layer1} is the air temperature of the layer 1, T_{layer2} is the air temperature of the layer 2, T_{layer3} is the air temperature of the layer 3, T_{layer4} is the air temperature of the layer 4, T_{am} is the air temperature of ambient, T_{out} is the air temperature of the outlet.

3.2. Selection of key structural parameters

The structural schematic diagram of the GSPW is presented in the left of Fig. 2. The following five dimensionless parameters (height ratio H^*, featured thickness δ^*, porosity σ, corrugated convexity L_w, and wave degree w^*) were initially identified as the key structural parameters affecting the thermal performance based on literature research, heat transfer analysis and simulation studies [35–37]. Among them, H^* visually reflects the proportionality of the perforated section to the absorber plate, δ^* represents the ratios of the channel to the hydraulic diameter, σ relates to the porosity to the heat transfer area, L_w shows the tangential relation of the corrugation protrusion angle, and w^* represents the individual wave to the width of the absorber plate.

$$H^* = Np/H \quad (9)$$

where, N is the row number of vertical holes, p is the distance of each hole, H is the total height of the device.

$$\sigma = nR^2 \sin\theta \Big/ HL \quad (10)$$

where, n is the total number of holes, R is the hole radii, θ is the corrugate angle, L is the total length of the GSPW.

$$\delta^* = \delta/D \quad (11)$$

where, δ is the thickness of the GSPW, D is the hydraulic length of the device.

$$L_w = 2W/l \quad (12)$$

where, W is the corrugate width, l is the corrugate length.

$$w^* = l/L \quad (13)$$

3.3. Simulation model

A 3D simulation model was created using Gambit 2.4.6. The grid is divided by structured hexahedron meshing, while the boundary layer mesh refinement is carried out around the outlet, the absorber plate and the holes. The maximum grid aspect ratio is 1:2.2, and the grid orthogonal quality exceeds 0.91 (ranging from 0 to 1, the closer to 0 the worse the grid quality is).

3.3.1. Simulation assumption

The thermal performance of the GSPW is influenced by the design parameters, operating conditions and environmental factors. Therefore, in order to simplify the calculation process, some reasonable assumptions need to be made: (1) air is an incompressible transparent medium and satisfies the Bossinesq assumption; (2) since the airflow is a low-speed incompressible flow, i.e., the heat dissipation caused by the work of the fluid

viscous force is neglected; (3) since the thickness of the absorber plate is small, the lateral thermal conductivity and thermal conductivity between the absorber plate and the shell can be ignored; (4) the long-wave radiation from the bottom of the absorber plate to the environment is disregarded due to the inlet opening.

3.3.2. Turbulence model and other settings

In this paper, FLUENT-3DDP 17.0 pressure-based 3D double precision solver is used for parallel transient solution, with the operation condition of default and considering the effect of gravity. A two-equation turbulence model is sufficient to meet the operational requirements and the Realizable k-ε model is used. The turbulence constants for high Reynolds number of small-hole jets should use the following values [38]:

$$\frac{\partial(\rho k)}{\partial \tau}+\nabla(\rho u k)=\nabla(\rho\{\mu_1+\mu_t/\sigma_k\})\nabla k+\rho(P_k-\varepsilon) \tag{14}$$

where, ρ is the air density, k is the turbulence kinetic energy, u is the air velocity component in corresponding direction, μ is the eddy viscosity, P_k is the generation of turbulence kinetic energy due to the mean velocity gradients, ε is the turbulence dissipation.

$$\frac{\partial(\rho \varepsilon)}{\partial \tau}+\nabla(\rho u \varepsilon)=\nabla(\rho\{\mu_1+\mu_t/\sigma_\varepsilon\})\nabla \varepsilon +\rho\left(C_{1\varepsilon}S\varepsilon-C_2\varepsilon^2\Big/\left\{k+\sqrt{(\mu_1\varepsilon)}\right\}\right) \tag{15}$$

$$\mu_t=C_\mu k^2\Big/\varepsilon \tag{16}$$

where, $C_{1\varepsilon}=1.44$, $C_2=1.9$, $C_\mu=0.09$, $\sigma_k=1.0$, $\sigma_\varepsilon=1.2$. The energy and wall Prandtl number is 0.85 because there is no supersonic flow. The wall boundary increases the accuracy by selecting the enhanced wall function. The value of y+ is found to be within 1 according to the calculation, which satisfies the function requirement. The radiation model selected is the DO model. The solar radiation IR is chosen as a single heat source, the radiation direction is positive y-axis, the Theta/Phi Divisions are both 4, and the Theta/Phi Pixels are both 2.

The material properties remained consistent with the experiments as shown in Table 1. Based on convergence time and resultant tests, solver settings are as follows: pressure-velocity coupling using SIMPLEC algorithm, based on the control body center method for gradient, pressure selection PRESTO! discrete format to increase jet accuracy, the rest of the term for the second-order windward format to increase the calculation accuracy. The convergence accuracy of all terms is $1e^{-03}$ except for the convergence accuracy of the energy equation, which is $1e^{-06}$. The transient time step is set to 10s and the number of iteration steps is 1000. Advance one time step after reaching convergence accuracy or maximum number of convergence steps.

3.3.3. Boundary conditions

The boundary conditions of the simulation follow the experimental setup as follows:

(1) The inlet is the pressure inlet boundary, the total pressure is 0 Pa, the incoming temperature is determined by conditions, the size is 200 × 100 mm^2 square;
(2) The outlet is fan suction, in order to guarantee the stability of the negative pressure wind speed. The reverse velocity inlet boundary is selected to realize the actual outlet situation, the size is 200 × 100 mm^2;
(3) The acrylic plate is 1300 × 600 × 5 mm^3, with convection radiation mixed wall boundary and semi-transparent radiation boundary. With convection heat transfer coefficient according to Eq. (17), sky radiation source temperature referred to Eq. (18), the radiation heat transfer coefficient is shown in Eqs. (19) and (20) [15];
(4) The heat collection plate is 1300 × 600 × 0.5 mm^3, with flow-solid coupling boundary and gray body aluminum material. The thermal conductivity of aluminum is high, so it is necessary to set Shell Conduction to fully consider the longitudinal thermal conductivity;
(5) The shell and air ducts are convection wall boundary with a thickness of 10 mm;
(6) The holes are interior infiltration boundary with a horizontal spacing of 60 mm and a vertical spacing according to Eq. (10);
(7) The outer wall is 120 mm thick with Neumann boundary conditions and a convection heat transfer coefficient according to Eq. (21) [19].

$$h_{c,g-am}=5.62+3.9U_\infty \tag{17}$$

where, U is the ambient air velocity, k is the turbulence kinetic energy, u is the air velocity component in corresponding direction, μ is the eddy viscosity, P_k is the generation of turbulence kinetic energy due to the mean velocity gradients, ε is the turbulence dissipation.

$$T_{sky}=0.0552\cdot T_{am}^{1.5} \tag{18}$$

$$h_{r,g-sky}=\varepsilon_g\sigma_b\left[T_g(\tau)+T_{sky}(\tau)\right]\left[T_g^2(\tau)+T_{sky}^2(\tau)\right] \tag{19}$$

$$h_{r,g-gound}=\varepsilon_g\sigma_b\left[T_g(\tau)+T_{gound}(\tau)\right]\left[T_g^2(\tau)+T_{gound}^2(\tau)\right] \tag{20}$$

$$h_{c,g-am}=5.62+3.9U_{room} \tag{21}$$

where, U_∞ is the ambient air velocity, U_{room} is the room air velocity, σ_b is the Bolfzmann constant, T_{sky} is the sky temperature, T_{ground} is the ground temperature.

3.3.4. Operating conditions setting

In purpose to investigate the impact law of different parameters on thermal efficiency and exergy efficiency, the simulations are performed as shown in Table 2 and Table 3:

Table 1
Material physical properties.

Properties	Material	Density	C_p	Conductivity	Absorbance/Transmittance
Fluid	Air	Bossinesq	1006.43	0.2	0.05/0.95
Acrylic plate	Polymethyl methacrylate	2250	830	1.15	0.1/0.9
solar absorber plate	Pure aluminum plate	2719	871	202.4	0.9/0
Outer wall	Brick-concrete composite material	2000	1200	0.1	0.043/0
Insulation shell	Wood	700	2310	0.173	0.1/0
Ventilation duct	Steel	8030	502.48	16.27	0.75/0

Table 2 shows the sensitivity analysis on environmental and structural parameters while other operating parameters constant. Each group has 9 parameters with the same difference between variables, for a total of 72 sets of operating conditions. Basically covering the intervals where the rate of change is more pronounced.

Table 3 is conducted to investigate the influence of the structure on the thermal efficiency under different air supply methods. The five variables of five structural parameters with three airflow conditions are simulated. A total of 3*5*5 = 75 sets of operating conditions, which basically cover the coupling influence law of structural parameters under low airflow to high airflow.

3.4. Comparison of simulation and experimental results

In order to investigate the effect of grid size on the discrete error of the computational results, a grid independence investigation is required. According to the GCI grid discretionary error analysis proposed by Celik [39], the correlation between the grid and the results can be evaluated. The results are shown in Table 4, where N_1, N_2, and N_3 represent the total number of three grid cells, respectively, and r_{21} and r_{32} represent the ratio of the average cell length of the grid (generally, three grids with a ratio greater than 1.3 are selected in the research). As defined in Equation (24), η_e is the equivalent thermal efficiency, and GCI_{fine}^{21} represents the discrete error, with smaller values being closer to the actual equations. Fig. 3 shows the variation of the physical field in the middle of channel-1 with the grid. It is noticed that the results of grid 1 are the most approximated to the extrapolated values, which is the computational limit that can be reached at this setting in the RNS simulation. Thus, the number of grids is chosen 1641860 for the final calculation and the deviation is acceptable.

The simulation results need to be compared with the experimental results to verify the accuracy of the CFD setup and turbulence model [40]. The air flow velocity and the temperature of each part in the cavity were compared under the same conditions and the deviation distribution is shown in Fig. 4. The middle line represents the 0 deviation between experiment and simulation, including the above interval where the simulation is larger than the experiment and below interval where the experiment is larger. The comparison results between experiment and simulation are indicated by the cases where the dots fall in the interval. It is found that the maximum error of wind speed is less than 8.6% while the maximum error of temperature is less than 8.9%. Therefore, the required accuracy requirement of the simulation setup can be satisfied, and the simulation results are considered realistic and credible.

3.5. Thermal efficiency and evaluation indexes of GSPW

The GSPW without auxiliary heat sources cannot operate all day since solar energy is intermittent. The exact operating times are determined by various regions, weather conditions and building functional requirements. Considering the actual operation performance of GSPW, it is also necessary to evaluate the application effectiveness in relation to the building type. The equations are expressed as follows:

The temperature rise ΔT is the transient difference between the outlet air temperature and the inlet air temperature (°C):

$$\Delta T = T_{out}(\tau) - T_{am}(\tau) \tag{22}$$

The heat collection efficiency η is the ratio of the total heat absorbed by the air through the absorber plate to the intensity of solar radiation, and its integral efficiency during the operation period is expressed [41]:

$$\eta = \frac{m_a(\tau)c_a[T_{out}(\tau) - T_{am}(\tau)]}{I(\tau)A_{p-sun}} \tag{23}$$

During the operation of the GSPW, the mechanical fan draws extra energy to pull the airflow into holes and to convert heat at the boundary layer. The mechanical and heat do not have the same energy level [42]. Thus, the energy and effective efficiencies of GSPW are defined as follows based on the first law of thermodynamics [43]. The equivalent thermal efficiency is obtained from equation (24)-(26):

$$\eta_e = \frac{m_a(\tau)c_a[T_{out}(\tau) - T_{am}(\tau)] - rE_{fan}(\tau)}{I(\tau)A_{p-sun}} \tag{24}$$

$$r = \frac{1}{C_{fan}} = \frac{Ethermal(\tau)}{Efan(\tau)} \tag{25}$$

$$Efan = \frac{m_a(\tau)KP_{drop}(\tau)}{\rho_a(\tau)\eta_f\eta_s} \tag{26}$$

where, E_{fan} is the wind mechanical power, K is the motor capacity reserve factor, η_f is the intra-fan efficiency, η_s is the mechanical efficiency, P_{drop} is the pressure drop in machine, C_{fan} is the conversion factor for converting different efficiencies (thermal to mechanical) and r is its derivative generally taken as 5. Taking into full consideration the effect of different fans, an alternative approach is via exergy analysis (i.e., the second law efficiency) [44], which is obtained from equation (27):

$$\eta_2 = \frac{m_a(\tau)c_a\left[\left(T_{out}(\tau) - T_{am}(\tau)\right) - T_{am}(\tau)\ln\left(T_{out}(\tau)/T_{am}(\tau)\right)\right] - E_{fan}}{I(\tau)A_{p-sun}\left[1 - \frac{4T_{am}(\tau)}{3T_{sun}(\tau)} + \left(\frac{1}{3}\right)\left(\frac{T_{am}(\tau)}{T_{sun}(\tau)}\right)^4\right]} \tag{27}$$

Heat loss rate η_{loss} is used to reflect the ratio of heat loss to total energy of the device [45]:

$$\eta_{loss} = \frac{\left[Q_{conv,g-am}(\tau) + Q_{rad,g-sky}(\tau) + Q_{rad,g-gound}(\tau)\right]}{I(\tau)A_{p-sun}} \tag{28}$$

The purpose of GSPW is to preheat the fresh air, so the fresh air infiltration heat load is emphasized. The equations of building instantaneous fresh air infiltration heat load Q_{load} and fresh air heat load elimination rate η_{load} are as follows [46]:

$$Q_{load} = m_a(\tau)c_a[T_n - T_{am}(\tau)] \tag{29}$$

$$\eta_{load} = \frac{m_a(\tau)c_a[T_{out}(\tau) - T_{am}(\tau)]}{Q_{load}} \tag{30}$$

Table 2
Selection for environmental and structural parameters.

Solar radiation intensity/W·m^{-2}	400	500	600	700	800	900	1000	1100	1200
Ambient temperature/°C	−30	−25	−20	−15	−10	−5	0	5	10
Environment wind speed/m·s^{-1}	0.5	1	1.5	2	2.5	3	3.5	4	4.5
Hole diameter/mm	2	3	4	5	6	7	8	9	10
Height radio H*	0.1	0.2	0.3	0.4	0.5	0.6	0.7	0.8	0.9
Featured thickness δ*	0.01	0.03	0.05	0.07	0.09	0.11	0.13	0.15	0.17
Corrugated convexity L_w	0.125	0.25	0.375	0.5	0.625	0.75	0.875	1	1.125
Wave degree w*	0.05	0.1	0.15	0.2	0.25	0.3	0.35	0.4	0.45

The heat storage capacity rate of the absorber plate is used to reflect the heat absorbed by the absorber plate but not exchanged:

$$\eta_{\mathrm{p-storage}} = \frac{c_{\mathrm{p}} M_{\mathrm{p}} \left[T_{\mathrm{p}}(\tau) - T_{\mathrm{p}}(0)\right]}{I(\tau) A_{\mathrm{p-sun}}} \tag{31}$$

The heat storage capacity rate of the air channel is used to reflect the heat storage in air channel, which ultimately maintains the heat balance of the solar wall:

$$\eta_{\mathrm{a-storage}} = 1 - \eta_{\mathrm{p-storage}} - \eta_{\mathrm{loss}} - \eta_{\mathrm{e}} - \eta_0 \tag{32}$$

Based on the above evaluation indexes, the performance of GSPW can be reasonably evaluated. Thus, its energy harvesting effect and heat transfer ratio can be judged to guarantee the structure optimization.

The energy efficiency indicates the ratio of the actual preheat of the device to the ideal preheat. The larger this value is, the better the energy saving effect of the device:

$$\eta_{\mathrm{saving}} = \frac{m_{\mathrm{a}} c_{\mathrm{a}} \Delta T}{m_{\mathrm{a}} c_{\mathrm{a}} (T_{\mathrm{n}} - T_{\mathrm{in}})} \tag{33}$$

Table 3
Selection for coupling structure with flow volume conditions.

Flow volume/m^3·h^{-1}	Hole diameter R/mm	Height radio H*	Featured thickness δ*	Corrugated convexity L_w	Wave degree w*
30	2	0.1	0.01	0.125	0.05
50	3	0.2	0.03	0.25	0.1
	4	0.3	0.05	0.375	0.15
80	5	0.4	0.07	0.5	0.2
	6	0.5	0.09	0.625	0.25

Table 4
Grid convergence index analysis.

N_1, N_2, N_3	r_{21}	r_{32}	η_e^1	η_e^2	η_e^3	p	η_{ext}^{21}	e_a^{21}	e_{ext}^{21}	GCI_{fine}^{21}
1641860, 629440, 277540	1.377	1.314	67.93%	67.99%	68.03%	0.478	67.58%	0.09%	0.52%	0.65%
	r_{21}	r_{32}	v_1 (m/s)	v_2 (m/s)	v_3 (m/s)	p	v_{ext}^{21} (m/s)	e_a^{21}	e_{ext}^{21}	GCI_{fine}^{21}
	1.377	1.314	0.071	0.068	0.059	4.427	0.072	3.97%	1.26%	1.59%
	r_{21}	r_{32}	T_1 (°C)	T_2 (°C)	T_3 (°C)	p	T_{ext}^{21} (°C)	e_a^{21}	e_{ext}^{21}	GCI_{fine}^{21}
	1.377	1.314	11.229	11.410	11.877	3.771	11.151	1.62%	0.70%	0.86%

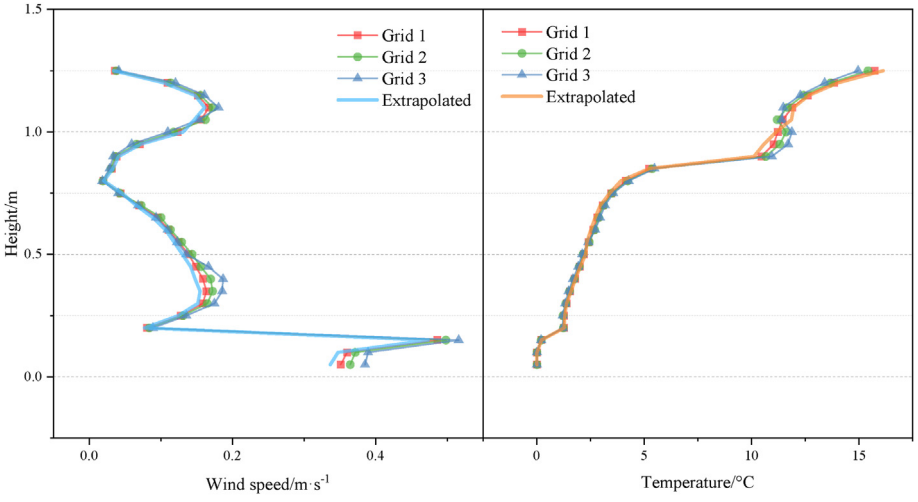

Fig. 3. Mesh independence verification in the channel-1.

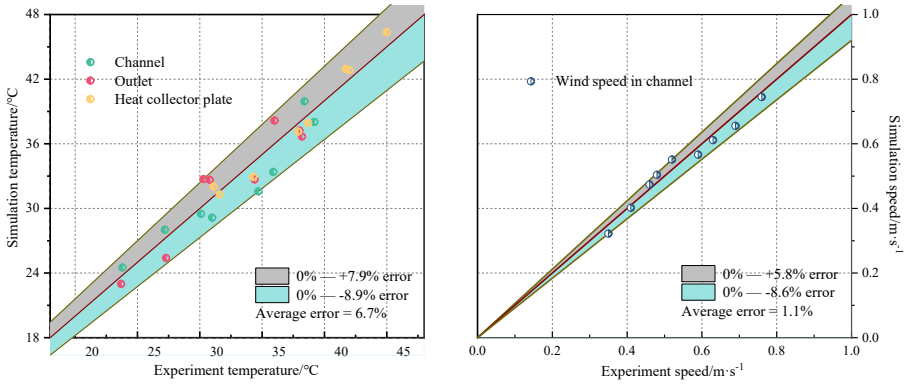

Fig. 4. Error comparison between simulation and experiment.

4. Results and discussion

4.1. Velocity vectors and temperature contours in GSPW

The velocity vectors and temperature contour plots of the GSPW are represented in Figs. 5a–5b. The mechanical force generated by the fan is originally oriented in the positive direction of the Y-axis. The airflow velocity and turbulence at the front of the absorber plate are larger, which is beneficial to the boundary layer heat transfer and minimize heat loss due to heat transfer to the glass. The mechanical force in channel-2 is opposite to the direction of the Z-positive buoyancy force. Therefore, a vortex secondary flow will be generated when the mechanical Z-axis partial pressure at the top of channel-2 is less than the floating lift force. As the height decreases, the difference between the two forces becomes smaller, resulting in smaller and smaller secondary flow vortexes until they disappear. In addition, the jet converges at the valley of the corrugated plate as a single vortex. The double vortex is generated at the wave peak due to the mutual interference of the left and right hole jets. Therefore, the corrugated plate will not only increase the heat transfer area but also increase the convective heat transfer through vortex.

The temperature field is the resultant characterization of fluid heat transfer. The cold air flow enters channel-1 with an initial velocity of 0.5 m/s. Since the channel is only 0.1 m, the cold air is transferred directly to the absorber plate and is heated. Afterwards, the warmer air rises along the absorber plate and mixes with the hot air progressively. The temperature gradient in the channel-1 shows a positive and increasing variation along the Z-axis, and the gradient normal vector points to the absorber plate. The average temperature rise caused by non-penetration plate heat transfer is 6.5 K, while that with penetration plate heat transfer is up to 12.5 K. This indicates that the heat transfer effect is stronger

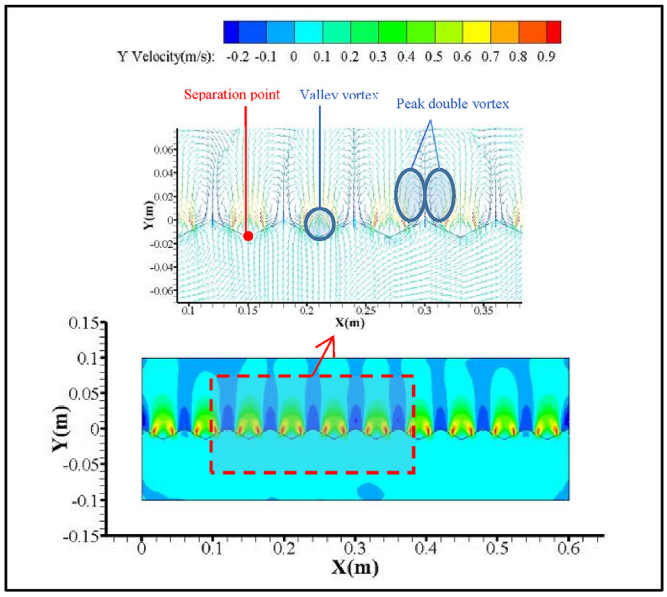

Fig. 5b. XY surface flow field characteristics (Z = 1.0m).

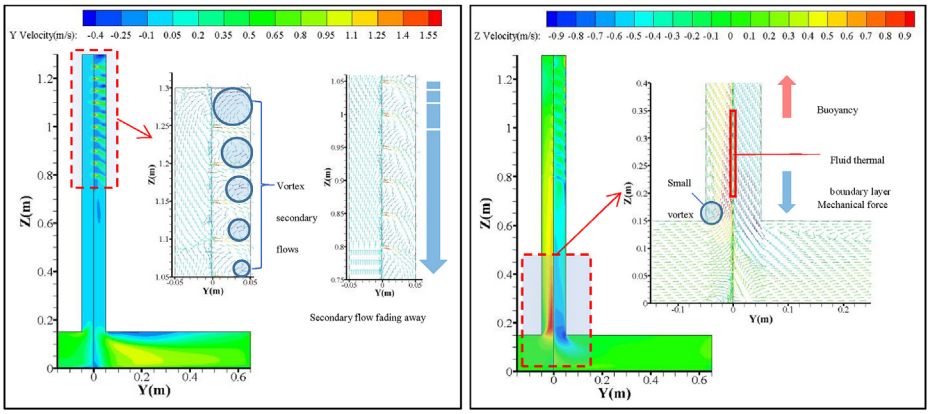

Fig. 5a. YZ surface flow field characteristics (X = 0.3m).

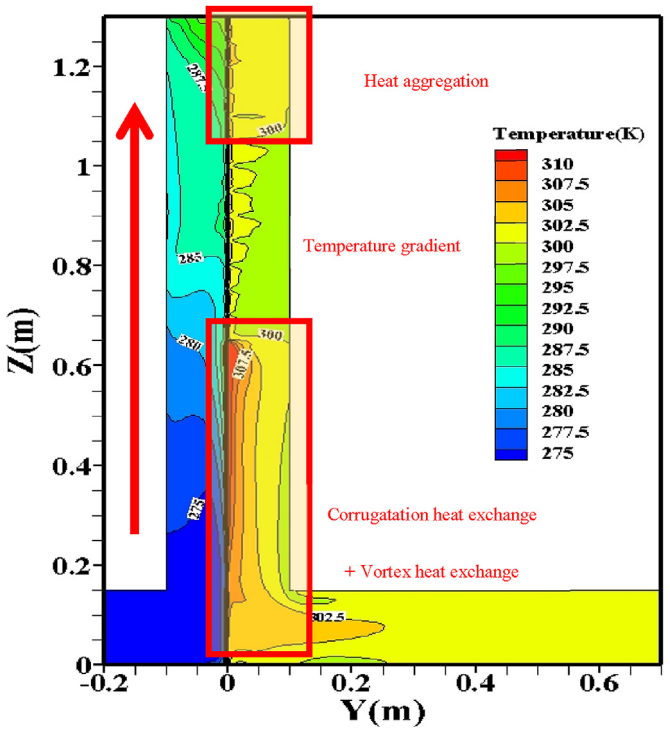

Fig. 5c. Temperature field characteristics (X = 0.3m).

near the penetration plate. The temperature field in channel-2 is more complex. The top is disturbed by the secondary flow while generating the temperature aggregation phenomenon. The gathered heat is transferred downward with shear stresses and secondary heat transfer occur due to the vortex. A temperature gradient decreasing along the Y direction is formed. It can be seen that enhancing the secondary heat exchange and reducing the heat accumulation are crucial to increase heat collection efficiency.

4.2. Influence of structural parameters on the thermal efficiency of GSPW

The structure parameters are important to affect the thermal performance of GSPW. It is mainly manifested in the variation of pressure drop and channel turbulence. This paper provides a reference for optimization by studying the relationship between thermal performance evaluation indexes and structure parameters.

4.2.1. Effect of hole diameter on thermal efficiency

The holes in the solar absorber plate are the only means of airflow from channel-1 to channel-2 in the GSPW. It causes the pressure difference to increase exponentially with the decrease of the hole diameter R. The variation of the thermal efficiency of the system with R is described in Fig. 6. The flow boundary layer and the cavity airflow are greatly disturbed due to the jet and suction effect of the small penetrations. The heat transfer coefficient is clearly positively correlated with the intensity of the pumping and jets, so the heat collection efficiency is negatively correlated with the variation of R. When R is 4 mm, the maximum equivalent thermal efficiency is 69.4% of the total energy when r is 1. However, when the electrothermal ratio r is also considered, the change of equivalent thermal efficiency appears to be extremely large. Due to the coupling effect between the r and R, the optimal R value increases with r. When r is range of 1–2, the optimal R is 0.003; when r is range of 3–5, the optimal R is 0.004; when r is range of 6–8, the optimal R is 0.006. Therefore, the structural design of R must be jointly matched the rated electrothermal ratio of the motor, otherwise there will be a maximum energy efficiency waste of 50%.

4.2.2. Effect of other structural parameters on thermal efficiency

The variation in total pressure drop is low with other structural parameters that the results can be discussed together in Fig. 7.

The uniform opening of the penetration is no longer suitable for the heat transfer requirements of GSPW, so the height ratio H^* becomes an important factor affecting the heat transfer efficiency. When H^* is small, the area of penetration plate is too small to meet the demand of increasing convection. On the contrary, when H^* is too large, the airflow is likely to flow to the outlet without sufficient heat exchange. The best value of heat collection efficiency is 0.68, the maximum heat collection is 318.3 W with the maximum temperature rise is 19.3 °C when H^* is 0.5. The amount of heat loss decreases with an increase of the height ratio.

The featured thickness δ^* directly affects the turbulence of the channel under the premise of a certain air volume. The turbulence increases as δ^* decreases. When δ^* is less than 0.13, the heat collection efficiency and the equivalent thermal efficiency are negatively correlated with δ^*. The maximum heat collection is

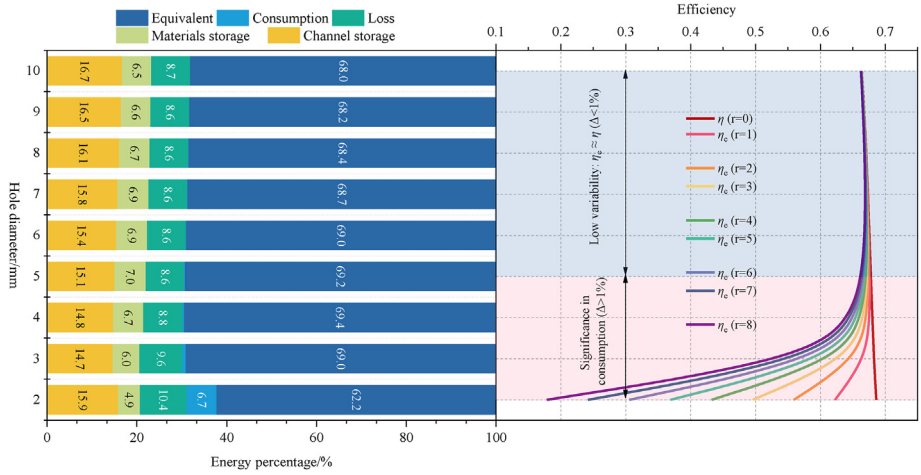

Fig. 6. Variation of thermal efficiency and energy percentage with hole diameter (H^* = 0.5, δ^* = 0.1, L_w = 1, w^* = 0.1, I = 600W/m^2, T_{am} = 0 °C, v_{am} = 3 m/s).

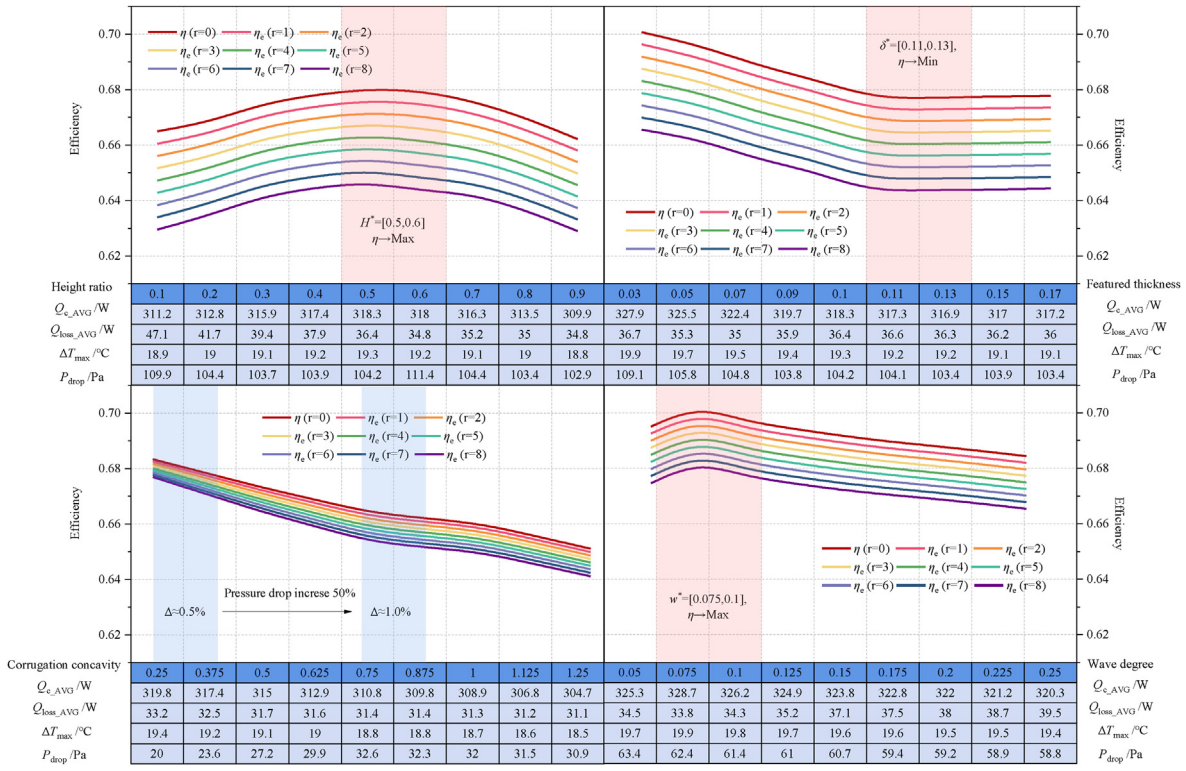

Height ratio	0.1	0.2	0.3	0.4	0.5	0.6	0.7	0.8	0.9	0.03	0.05	0.07	0.09	0.1	0.11	0.13	0.15	0.17
Q_{c_AVG} /W	311.2	312.8	315.9	317.4	318.3	318	316.3	313.5	309.9	327.9	325.5	322.4	319.7	318.3	317.3	316.9	317	317.2
Q_{loss_AVG} /W	47.1	41.7	39.4	37.9	36.4	34.8	35.2	35	34.8	36.7	35.3	35	35.9	36.4	36.6	36.3	36.2	36
ΔT_{max} /°C	18.9	19	19.1	19.2	19.3	19.2	19.1	19	18.8	19.9	19.7	19.5	19.4	19.3	19.2	19.2	19.1	19.1
P_{drop} /Pa	109.9	104.4	103.7	103.9	104.2	111.4	104.4	103.4	102.9	109.1	105.8	104.8	103.8	104.2	104.1	103.4	103.9	103.4

Corrugation concavity	0.25	0.375	0.5	0.625	0.75	0.875	1	1.125	1.25	0.05	0.075	0.1	0.125	0.15	0.175	0.2	0.225	0.25
Q_{c_AVG} /W	319.8	317.4	315	312.9	310.8	309.8	308.9	306.8	304.7	325.3	328.7	326.2	324.9	323.8	322.8	322	321.2	320.3
Q_{loss_AVG} /W	33.2	32.5	31.7	31.6	31.4	31.4	31.3	31.2	31.1	34.5	33.8	34.3	35.2	37.1	37.5	38	38.7	39.5
ΔT_{max} /°C	19.4	19.2	19.1	19	18.8	18.8	18.7	18.6	18.5	19.7	19.9	19.8	19.7	19.6	19.6	19.5	19.5	19.4
P_{drop} /Pa	20	23.6	27.2	29.9	32.6	32.3	32	31.5	30.9	63.4	62.4	61.4	61	60.7	59.4	59.2	58.9	58.8

Fig. 7. Variation of heat collection efficiency and equivalent thermal efficiency with height ratio (R = 4 mm, I = 600W/m^2, T_{am} = 0 °C, v_{am} = 3 m/s).

327.9 W with the maximum temperature rise of 19.9 °C as δ* is the minimum. This is due to the appearance of large vortexes in the channel. As δ* continues to increase, the thermal efficiency tends to stabilize. At this point, the heat transfer mechanism in the GSPW channel is equivalent to that of a normal UTC.

The corrugation concavity L_w affects the vortex flow field of the corrugated inner wall, which affects the effect of heat transfer. It is found that the heat collection efficiency decreases with the increase of L_w. The increase of the heat transfer area makes the temperature of the absorber plate decrease, thus the convective heat transfer is reduced by about 3%. The maximum heat collection is 319.8 W with the maximum temperature rise of 19.4 °C as L_w is the minimum. In addition, the difference in the equivalent thermal efficiency between the different electrothermal ratios increases with the increase in corrugation bump, from a total of 0.65%–1.00%.

The wave degree w* is the main factor affecting the turbulence degree. The change of the heat collection efficiency and equivalent thermal efficiency tend to be the same and both have extreme values at w* of 0.075. This is due to the fact that when w* is too small, the spacing between the crests is too close to each other resulting in enhanced mutual disturbance between the vortexes. Conversely, the vortexes in the trough disappear leading to a decrease in the perturbation and thus a change in the convective heat transfer coefficient.

4.3. Coupling effect of air volume and structural factors on heat and exergy efficiency

The turbulence degree in the channel is influenced by both wind speed and structural parameters, while the wind speed is determined by the fresh air demand. The design is based on the primary premise of ensuring the fresh air volume, the main objective of improving the thermal efficiency and the efficiency of the chamber, and the turbulence degree in the cavity as the associated variable. Therefore it is crucial to determine the coupling relationship between air volume and structural parameters. In this paper, three air volumes (30, 50 and 80 m^3/h) are selected to correspond to the required fresh air volume selection in a single room due to different functions.

4.3.1. Coupling effect of porosity on heat and exergy efficiency

The coupled variation of equivalent thermal efficiency with air volume V and porosity σ can be obtained from Fig. 8. Three regions are used to represent the changes in efficiency due to coupling, where I is the weakened region, II is the smooth region, and III is the enhanced region. Zones I and II show that large V and small σ cause a sharp decrease in efficiency. However, this change only occurs when σ is less than 0.002 and the efficiency gradient becomes more pronounced as σ decreases. As the σ becomes larger, the equivalent thermal efficiency increases steadily with an increase of V. This is very different from the results in Section 4.2. The reason for this phenomenon is that the low V makes the pumping effect of small σ no longer obvious. The weakened flow in the channel makes the temperature aggregation more pronounced. The decrease in σ causes an increase in turbulence in the vortex at the top of channel-2. Conversely, an increase in porosity causes a weakening of the exit suction. The variation of exergy efficiency is diametrically opposite to the heat efficiency. However, as the σ increases, the difference becomes smaller. Due to the excessive power consumption, the revenue exergy cannot meet the payment demand. Therefore, it leads to additional exergy loss making the operation of the solar wall meaningless. In summary, if the design does not consider the coupling relationship between porosity and air volume, the exergy efficiency becomes negative, i.e., additional exergy loss is generated.

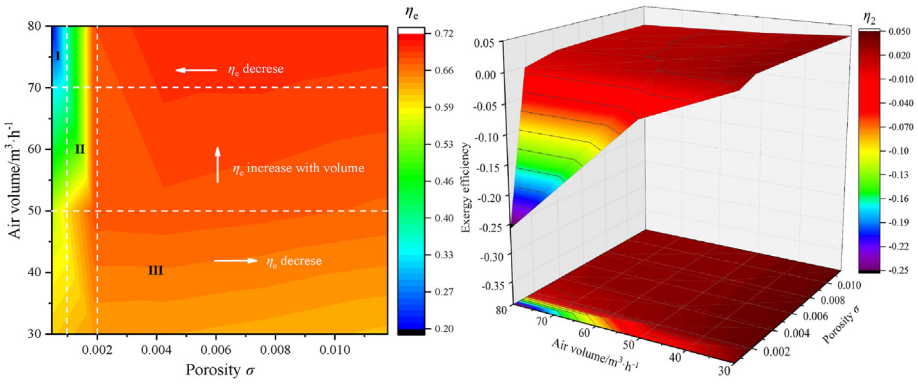

(a) equivalent thermal efficiency (b) exergy efficiency

Fig. 8. Variation of thermal efficiency with porosity
(H^* = 0.5, δ^* = 0.1, L_w = 1, w^* = 0.1, I = 600W/m^2, T_{am} = 0 °C, v_{am} = 3 m/s).

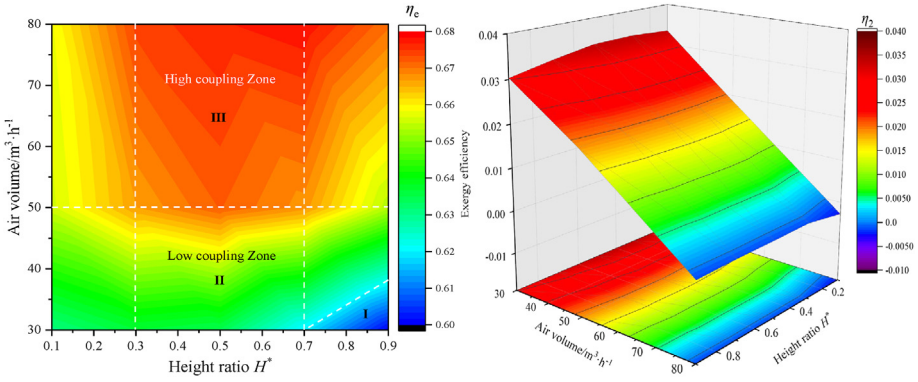

(a) equivalent thermal efficiency (b) exergy efficiency

Fig. 9. Variation of thermal efficiency with height ratio
(D = 4 mm, δ^* = 0.1, L_w = 1, w^* = 0.1, I = 600W/m^2, T_{am} = 0 °C, v_{am} = 3 m/s).

4.3.2. Coupling effect of height ratio on heat and exergy efficiency

There is no strong correlation between the height ratio H^* and the pressure difference in section 4.2. However, according to Fig. 9 it can be seen that the equivalent thermal efficiency increases from 0.2% to 3.4% with an increase of the airflow V. This is caused by the increase in the equivalent electrical heating rate, which is clearly not consistent with the results in section 4.2. Zone I shows that large V with H^* causes a significant decrease in efficiency. The only explanation is that the increase in airflow affects the numerical relationship between H^* and the pressure drop. Therefore, it can be proved that there is a strong coupling relationship between V and H^*. In addition, it can be found that the optimal H^* becomes 0.3, 0.5, and 0.7 for V of 30, 50, and 80 m^3/h. It can be understood that the increase of V can reduce the problem of insufficient heat transfer in the airflow generated by the heat collection penetration plate, thus allowing a higher percentage of penetration plate. The change of exergy efficiency is diametrically opposite to the heat efficiency. Additional exergy losses will be generated at high V, again caused by additional electrical heat work. Exergy efficiency varies in the same way as thermal efficiency at a higher rate with H^* at low V. Therefore, the focus is on the need for a reasonable value of the height ratio at lower airflow operation.

4.3.3. Coupling effect of featured thickness on heat and exergy efficiency

There is no strong correlation between the δ^* and the differential pressure. However, it can be found that the change of V causes a dramatic change in thermal efficiency with the variation pattern of δ^* in Fig. 10. The most obvious one is that when δ^* is greater than 0.10, the equivalent thermal efficiency increases firstly and then decreases with V below 40 m^3/h. When the V beyond 50 m^3/h, the equivalent thermal efficiency decreases firstly and then remains unchanged. This is because the δ^* and V can change the channel turbulence, and there is a more obvious coupling relationship. The variation of exergy efficiency is still opposite to that of heat collection efficiency. The exergy efficiency changes more smoothly as the V increases. In general, the variation of exergy efficiency with δ^* is small, so only the effect of thermal efficiency can be considered in the selection.

4.3.4. Coupling effect of corrugation convexity and wave degree on heat and exergy efficiency

There is a weak correlation between the corrugation convexity L_w and the differential pressure according to section 4.2. According to Table 4, it can be found that the change of V does not cause a large change in the thermal efficiency with the variation pattern of L_w. Only the slope of change decreases with the increase of V, and what needs attention is the choice of the structure of L_w at low air volume. The exergy efficiency decreases with increasing V and is negatively correlated with the L_w. In summary, the coupling relationship between V and L_w is not very obvious and can be ignored or considered as appropriate.

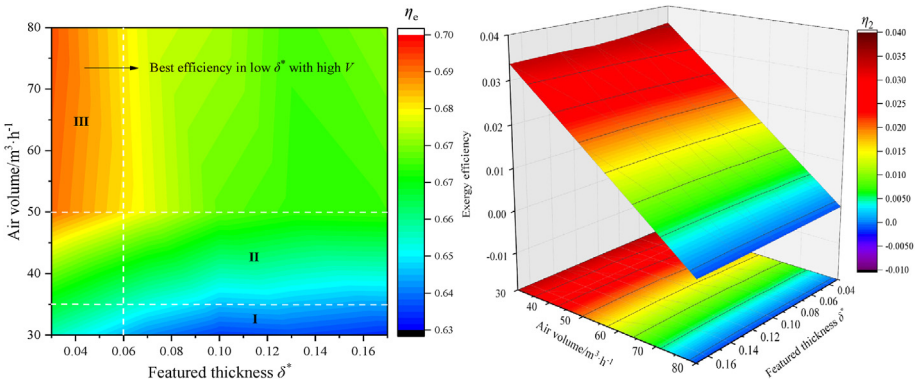

(a) equivalent thermal efficiency (b) exergy efficiency

Fig. 10. Variation of thermal efficiency with featured thickness (H^* = 0.5, D = 4 mm, L_w = 1, w^* = 0.1, I = 600W/m^2, T_{am} = 0 °C, v_{am} = 3 m/s).

Table 5
Variation of thermal efficiency with corrugation convexity and wave degree.

L_w	V (m^3/h)	η (%)	η_e (%)	η_2 (%)	w^*	V (m^3/h)	η (%)	η_e (%)	η_2 (%)
0.25	30	64.91	64.87	3.60	0.05	30	65.43	65.31	3.61
0.5	30	63.18	63.13	3.40	0.1	30	65.61	65.50	3.63
0.75	30	61.70	61.64	3.25	0.15	30	65.39	65.28	3.61
1	30	61.13	61.07	3.19	0.2	30	65.20	65.10	3.59
1.25	30	60.05	59.99	3.08	0.25	30	65.06	64.95	3.58
0.25	50	68.33	68.17	2.38	0.05	50	69.51	69.00	2.28
0.5	50	67.31	67.09	2.28	0.1	50	69.70	69.20	2.30
0.75	50	66.40	66.14	2.19	0.15	50	69.19	68.70	2.27
1	50	66.01	65.75	2.17	0.2	50	68.92	68.44	2.25
1.25	50	65.11	64.86	2.11	0.25	50	68.66	68.18	2.24
0.25	80	70.65	69.99	1.32	0.05	80	72.15	70.10	0.65
0.5	80	69.92	69.02	1.16	0.1	80	72.25	70.26	0.69
0.75	80	69.12	68.04	1.03	0.15	80	71.90	69.94	0.69
1	80	68.50	67.45	1.02	0.2	80	71.40	69.49	0.69
1.25	80	67.87	66.86	1.01	0.25	80	71.17	69.27	0.69

Similarly, there is no strong correlation between the wave degree w^* and the differential pressure. Similar to section 4.2, it can be seen that the change in V does not cause a large change in the pattern of thermal efficiency with w^*, although the rate of change in thermal efficiency is greater at high air volumes from Table 5. In addition, the exergy efficiency is negatively correlated with V, which is consistent with the trend of the thermal efficiency. In conclusion, the coupling relationship between air volume and w^* is not very obvious, and only the high air volume case can be considered.

4.4. Effect of environmental factors on exergy efficiency and heat loss rate of GSPW

Environmental factors are the main factors that cause exergy payment and the amount of heat loss, which in turn affects the efficiency of the solar wall and the heat loss rate. It also affects the energy acquisition conversion capacity and insulation performance of the system. The effect of environmental factors on exergy efficiency and heat loss rate of GSPW is shown in Fig. 11.

The exergy efficiency and heat loss rate increase with solar radiation intensity I and the growth rate decreases. This is because the large energy input leads to an increase in the temperature of the absorber plate and channels. The convective and radiant heat exchange on the surface of the glass plate and the shell will also increase. As a reference, the heat loss increment increased from 24 W to 220.8 W, an increment rate of about 9.2 times. And the exergy efficiency increased from 0.006 to 0.05, an increase of about 8.3 times. The heat loss increment is very large, so the design needs to consider the use of glass materials with low absorption rate and the shell needs to increase the insulation layer. In addition, the temperature increases linearly with the positive correlation of I, and the thermal efficiency increases significantly below I of 700 W/m^2.

The exergy efficiency of the system decreases with increasing ambient wind speed v_{am}, while the heat loss rate increases gradually and the rate of change is close to the same. This is because the convective heat transfer loss increases steadily with the increase of v_{am}. The average rate of change of heat loss rate with increasing unit wind speed is about 2.07%/m·s^{-1}. Thus, compared to UTC with the change in ambient wind speed from 1 m/s to 5 m/s the thermal efficiency decreases from 75% to 25% with heat loss up to 50% [19]. The change of heat loss of GSPW is only 8.3%, which greatly solves the interference of solar collectors by high side winds. In addition, it is known that the average exergy efficiency of GSPW is about 2.3%, while the maximum conventional GTC is only 1.8% [19]. Therefore, GSPW more excellent in terms of available energy harvesting.

The exergy efficiency decreases with increasing ambient temperature T_{am}. The heat loss rate follows a decreasing then increasing pattern and has a minimum value at T_{am} is −10 °C. This is because as T_{am} increases, the temperature difference is smaller and therefore the heat exchange rate and the available energy decreases. When T_{am} is low, the temperature difference is larger and the convective heat loss increases. It is found that the heat loss rate changes from a maximum of about 0.4% and the exergy efficiency decreases from 0.028 to 0.022. The temperature rise does not change with T_{am}, indicating that GSPW has no application limitations in cold regions. The thermal efficiency increases as T_{am} decreases, which further reflects the superior performance of GSPW in extremely cold regions.

4.5. Functional adaptation analysis of GSPW

The heat transfer flow mechanism, internal flow and temperature distribution, and structural optimization of solar walls have been basically studied in the above chapters. However, since the studies are conducted under steady state or constant design conditions. The needs of different regions and different functional buildings all have large differences, which require an extended analysis of application adaptability.

The heat load elimination rates of different functional buildings are shown in Fig. 12, and only building types in Xi'an area are considered in this section. With the increase of new air demand in

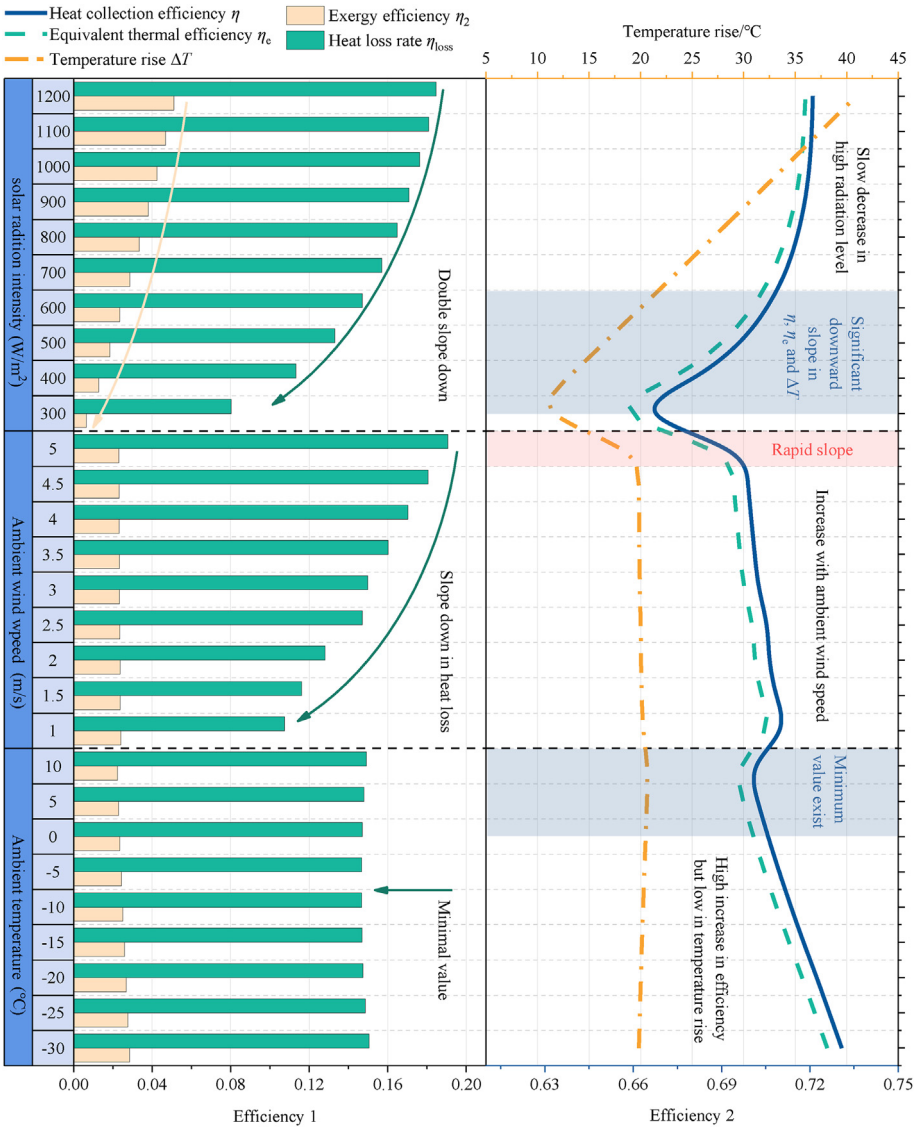

Fig. 11. Variation of thermal efficiency with solar radiation intensity ($H^* = 0.5$, $\delta^* = 0.1$, $L_w = 1$, $w^* = 0.1$, $D = 4$ mm).

different functional buildings, although the heat transfer efficiency is improved. However, the growth rate of new air infiltration load is greater, so the heat load elimination rate decreases. If a 75% time non-guarantee rate is considered, all buildings meet the load demand. If 50% of the time non-assurance rate is considered, the chemical room and kitchen cannot meet the load demand. If a 25% time default rate is considered, only the residential and office buildings can meet the load demand. Therefore, for different building types, the operation time needs to be followed up and adjusted, and auxiliary heat sources are considered to meet the heat demand according to the functional needs of the building. The optimal design solution can be roughly obtained according to the regional meteorological characteristics and building types, as shown in Table 6. This example is selected from Xi'an region, with a 9 m^2 solar wall and a single room with a floor area of 20 m^2. Although the difference is not significant, it is still possible to see the influence of different fresh air demand on the structural design, especially the two parameters of porosity and height ratio.

4.6. Energy saving potential of GSPW

In this paper, a GSPW with a transparent area of 9 m^2 is selected for energy analysis under real conditions. The region is chosen as Xi'an, China. The simulation time is from 07:00 to 17:00 on January 1, 2021 because only this time has sunlight. The initial ambient temperature is 268.8K and the maximum solar radiation is 504.5W/m^2. The energy captured with an air volume of 240 m^3 is shown on the left side of Fig. 13. The absorbed energy is lower than the solar energy due to the acrylic transmittance of 0.9 and the absorption coefficient of the collector plate of 0.9. It can be seen that the supplied energy grows half an hour later than the irradiation amount due to the collector plate preheating. With an increase of solar irradiation, the supplied energy keeps increasing until 15 o'clock. Afterwards the sun gradually falls, therefore utilized energy decreases to 0. In this process, the total solar energy is 30.3 kWh, the absorbed energy is 24.5 kWh, the supplied energy is 21.4 kWh, the unused amount is 8.9 kWh, and the energy loss is only 3.1 kWh.

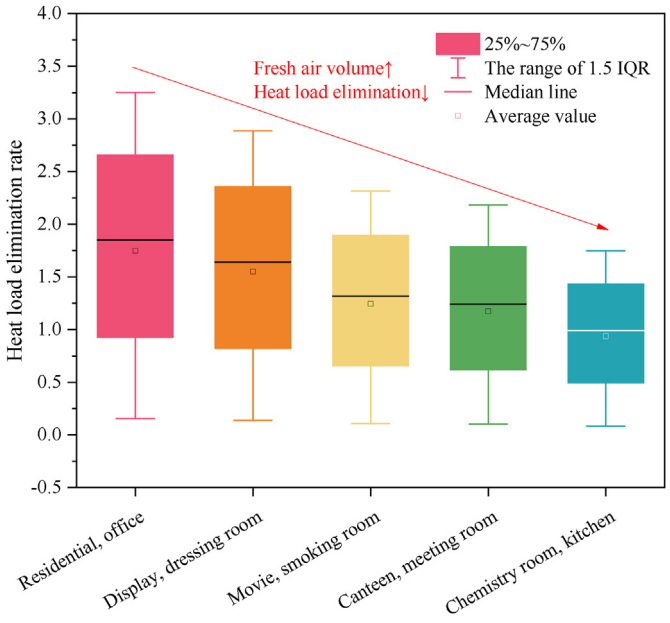

Fig. 12. Typical daily ambient temperature and solar radiation intensity in different regions
($H^* = 0.5$, $\delta^* = 0.1$, $L_w = 1$, $w^* = 0.1$, $D = 4$ mm).

Table 6
Optimal parameters for the specific buildings of Xi ' an.

Room type	V (m^3/h)	σ	H^*	δ^*	L_w	w^*	η	η_e	η_2
Residential	160	0.001	0.3	0.03	0.25	0.1	64.78%	64.66%	9.4%
Museum	240	0.002	0.3	0.03	0.25	0.1	68.13%	67.95%	6.9%
Cinema	400	0.003	0.4	0.03	0.25	0.1	70.76%	70.14%	4.6%
Restaurant	500	0.004	0.5	0.03	0.25	0.1	75.41%	74.52%	2.5%
Chemistry	700	0.005	0.5	0.03	0.25	0.1	78.39%	76.71%	1.6%

This shows that GSPW can supply energy efficiently and the energy gain per square meter is significant.

The variation of energy collection efficiency, energy transfer efficiency and energy saving efficiency for different air supply volumes are included on the right side of Fig. 13. The collection efficiency is limited to 0.81 by the material, while the transfer efficiency does not exceed 1. It is interesting to find that the collection efficiency and transfer efficiency increase with the air volume, while the energy saving efficiency decreases. This is because the air volume increases the turbulence with convection heat exchange. The temperature is lower and the heat loss is smaller, so the heat collection efficiency is increased. However, the lower air supply temperature not only leads to additional energy consumption when the temperature does not reach the standard, but also shortens the time interval for the temperature to reach the standard. As a result, although the energy supply is increased, the energy saving is no longer significant. Therefore, it is important to consider improving the energy saving advantage as well as continuously improving the heat collection efficiency. Energy saving efficiency over 1 indicates that there is excess heat and superheated air temperature, so it is also possible to consider adding energy storage equipment to expand its advantages.

5. Conclusion

In this paper, CFD simulation studies are conducted to investigate fluid flow and heat transfer in a GSPW. The GSPW structure is optimized and the application effects are investigated. The corresponding indexes for evaluating the thermal performance of the GSPW are proposed. The specific conclusions are drawn as follows:

(1) The corrugated non-penetration plate section forms a continuous flow boundary layer and generates vortexes at the frontal trough. In contrast, the corrugated hole plate section shows boundary layer separation at the small hole penetration and generates double vortexes at the back wave crest. The secondary flow exists at the top of channel-2 and fades downward, causing secondary flow and generating heat build-up phenomenon. Larger air volume and suitable height ratio can effectively attenuate this phenomenon.

(2) There is an obvious coupling relationship between air volume and porosity, height ratio and featured thickness. Large air volumes with low porosity can lead to significant reductions in both equivalent thermal efficiency and exergy efficiency, down to 20% and −25% respectively. A high air volume at a height ratio between 0.3 and 0.7 or a featured thickness below 0.06 will result in the highest range of equivalent thermal efficiency. Therefore, the design of structural parameters cannot refer to the sensitivity variation of single structural parameters. Otherwise, it will result in a maximum of 50% electric heat expenditure and 30% additional heat loss.

(3) By sensitivity analysis, the optimal structural parameters for thermal efficiency were obtained as a porosity of 0.2%, a height ratio of 0.55, a featured thickness of 0.12, a corrugation concavity of 0.25, and a wave degree of 0.875. The heat

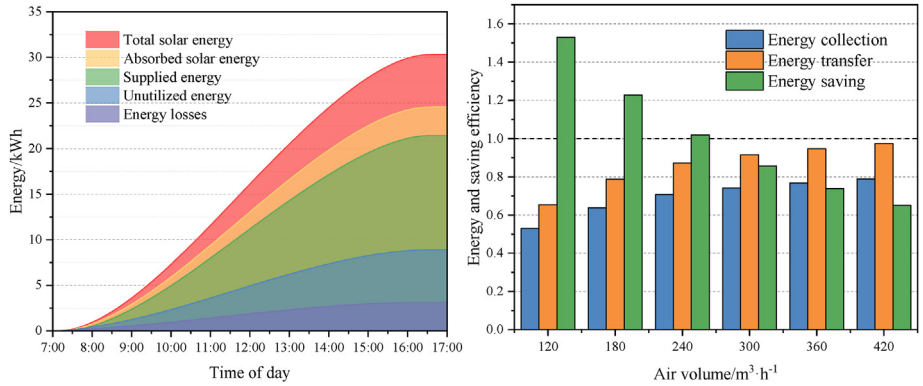

Fig. 13. Energy saving efficiency on different volume and daily energy supply
($A_p = 9$ m^2, $H^* = 0.5$, $\delta^* = 0.1$, $L_w = 1$, $w^* = 0.1$, $D = 4$ mm).

and exergy efficiency of GSPW is both 1.3 times higher than that of the traditional solar wall. The influence of environment on the heat loss rate does not exceed 8.3%, which indicates that GSPW not only improves the effective energy utilization rate, but also has better application prospects in extreme climate regions.

(4) The solar wall can effectively eliminate the fresh air infiltration load and at the same time reduce the building load through the heat storage and insulation effect. The load elimination rate is as high as 2–5 times and is best adapted in residential houses in Northwest China. The daily energy supply can reach 2.4 kWh/m^2 under an actual condition. The energy saving efficiency is greater than 1 at low air volume. Auxiliary heat sources and energy storage modules are necessary due to fluctuating temperatures.

(5) The optimal design parameters for different buildings in Xi'an are given in this paper as a summary of the parametric investigation. The most influential of the structural parameters are porosity and height ratio. The increase in air exchange demand from residential to chemical rooms leads to an increase in porosity while the height ratio converges to 0.5. The equivalent thermal efficiency increases from 64.7% to 76.7% and the exergy efficiency decreases from 9.4% to 1.6%.

However, there are certain limitations in this study. For example, the application of GSPW needs to set the auxiliary heat source according to the regional adaptation combined with a thermal storage, electricity and gas, in order to meet the indoor heat demand through intelligent control.

Declaration of competing interest

The authors declare that they have no known competing financial interests or personal relationships that could have appeared to influence the work reported in this paper.

Appendix

Nomenclature

Geometric symbols

A_{pl}	Non-perforated plate area (m^2)
A_{in}	Inlet area (m^2)
A_w	Wall area (m^2)
D	Feature length (m)
L	Horizontal length of absorber plate (m)
H	Height of absorber plate (m)
N	Number of vertical hole rows
R	Hole diameter (m)
W	Corrugated bump height (m)
H^*	Height ratio
δ^*	Featured thickness
θ	Corrugated angle (°)
A_{ph}	Perforated plate area (m^2)
A_g	Glass area (m^2)
$A_{p\text{-}sun}$	Area under direct sunlight (m^2)
l	Single corrugation width (m)
δ	Channel thickness (m)
p	Vertical hole spacing (m)
n	Total number of holes
δ_w	Thickness of wall (m)
σ	Porosity
L_w	Corrugation convexity
w^*	Wave degree

Physical symbols

α_p	Absorbance of solar absorber plate
β_g	Glass transmittance
ε_g	Emissivity of glass
c_a	Specific heat capacity of air (J/kg·K)
μ_a	Viscosity coefficient (kg/s·m)
c_p	Specific heat capacity of plate (J/kg·K)
α_g	Absorbance of glass
ε_p	Emissivity of solar absorber plate
ε_w	Emissivity of wall
ρ_a	Air density (kg/m^3)
σ_b	Boltzmann constant
M_p	Weight of absorber plate (kg)

Thermal symbols

T_g	Glass temperature (K)
T_{ph}	Perforated plate temperature (K)
T_{sky}	Sky temperature (K)
T_{ground}	Ground temperature (K)
T_{sun}	Sun temperature (K)
T_{out}	Outlet temperature (K)
k_p	Plate thermal conductivity (W/m·K)
h_c	Convection heat transfer coefficient
I	Solar radiation intensity (W/m^2)
Q_{conv}	Convection heat exchange (W)
Q_{rad}	Radiant heat exchange (W)
T_{pl}	Non-perforated plate temperature (K)
T_{am}	Ambient temperature (K)
T_{room}	Indoor temperature (K)
T_n	Room design temperature (K)
ΔT_n	Temperature rise (K)
k_w	Wall thermal conductivity (W/m·K)
k_a	Air thermal conductivity (W/m·K)
h_r	Radiant heat transfer coefficient
Q_{load}	Cold air infiltration load (W)
Q_{cond}	Heat conduction (W)
$E_{thermal}$	Motor thermal (W)

Flow symbols

U_∞	Ambient wind speed(m/s)
P_{drop}	Pressure drop (Pa)
η_f	Intra-fan efficiency
r	Equivalent electrothermal ratio
V_a	Volume flow (m^3/s)
U_{room}	Indoor wind speed (m/s)
K	Motor capacity reserve factor
η_s	Mechanical efficiency
m_a	Mass flow (kg/s)
E_{fan}	Motor power consumption (W)

Efficiency symbols

η_e	Equivalent thermal efficiency
η_{load}	Heat load elimination rate
η	Heat collection efficiency
$\eta_{p\text{-}storage}$	Heat storage capacity rate of plate
η_2	Exergy efficiency
η_{loss}	Heat loss rate
η_0	Equivalent electric heat rate
$\eta_{a\text{-}storage}$	Heat storage capacity rate of channel

Subscripts

pl-layer1	Corrugated plate to layer-1
ph-layer3	penetration plate to layer-3

g-layer1	Glass to layer-1
wi-layer3	Wall to layer-3
pl-g	Corrugated plate to glass
pl-wi	Corrugated plate to inner wall
pl-ph	Corrugated plate to penetration plate
g-am	Glass to ambient
wo-room	Outer wall to room
ph-layer2	penetration plate to layer-2
pl-layer4	Corrugated plate to layer-4
g-layer2	Glass to layer-1
wi-layer4	Wall to layer-4
ph-g	penetration plate to glass
ph-wi	penetration plate to inner wall
wi-wo	Inner wall to outer wall
g-sky	Glass to sky

References

[1] N. Somu, M.R.G. Raman, K. Ramamritham, A deep learning framework for building energy consumption forecast, Renew. Sustain. Energy Rev. (2021) 137.

[2] V.D. Amelija, M.R. Jasmina, V.V. Ana, R.M.N. Jelena, S.B.P. Ivana, Estimation of indoor temperature for a passive solar building with a combined passive solar system, J. Energy Eng. 143 (4) (2017), https://doi.org/10.1061/(ASCE)EY.1943-7897.0000437.

[3] Kumar Mithraratne, Brenda Vale, Modelling of thermal characteristics of insulated mass in zero-heating passive solar houses: Part 1 theoretical analysis, Architect. Sci. Rev. 49 (2006).

[4] S. Abhishek, A.A.E. Varun, A Thermodynamic Review of Solar Air Heaters. Renewable and Sustainable Energy Reviews, vol. 43, 2015.

[5] K. P, M.S. C, B. A, F. J, Optimized finned absorber geometries for solar air heating collectors, Sol. Energy 67 (1999).

[6] P.K. Bansal, S.C. Kaushik, Diurnal Response of Solar Air Heaters, vol. 9, Elsevier, 1981.

[7] B. Li, S. You, T. Ye, H. Zhang, X. Li, C. Li, Mathematical modeling and experimental verification of vacuum glazed transpired solar collector with slit-like perforations, Renew. Energy 69 (2014) 43–49.

[8] X. Li, C. Li, B. Li, Net heat gain assessment on a glazed transpired solar air collector with slit-like perforations, Appl. Therm. Eng. 99 (2016) 1–10.

[9] A. Ae, S. A, M. Rir, S. MS, B. MM, Thermal performance investigation of double pass-finned plate solar air heater, Appl. Energy 88 (2010).

[10] C. C, P. Mc, H. Pg, Design curves for conventional solar air heaters, Renew. Energy 6 (1995).

[11] R. Vaziri, M. Ilkan, F. Egelioglu, Experimental performance of perforated glazed solar air heaters and unglazed transpired solar air heater, Sol. Energy 119 (2015) 251–260.

[12] W. Zheng, B. Li, H. Zhang, S. You, Y. Li, T. Ye, Thermal characteristics of a glazed transpired solar collector with perforating corrugated plate in cold regions, Energy 109 (2016) 781–790.

[13] W. Zheng, H. Zhang, S. You, Y. Fu, X. Zheng, Thermal performance analysis of a metal corrugated packing solar air collector in cold regions, Appl. Energy 203 (2017) 938–947.

[14] X. Li, S. You, H. Zhang, G. Lin, Study on influence factors of thermal performance of glazed transpired collector with slit-like perforation, Acta Energiae Solaris Sin. 33 (2012) 928–936.

[15] M.R. Hooman, A. Mehran, Energy and exergy study of unglazed transpired collector-2stage, Sol. Energy 132 (2016).

[16] B. Brij, S. Ranjit, Thermal and thermohydraulic performance of roughened solar air heater having protruded absorber plate, Sol. Energy 86 (2012).

[17] T. Zhang, Y. Tan, X. Zhang, Z. Li, A glazed transpired solar wall system for improving indoor environment of rural buildings in northeast China, Build. Environ. 98 (2016) 158–179.

[18] D. Eryener, J. Hollick, H. Kuscu, Thermal performance of a transpired solar collector updraft tower, Energy Convers. Manag. 142 (2017) 286–295.

[19] L. Gao, H. Bai, S. Mao, Potential application of glazed transpired collectors to space heating in cold climates, Energy Convers. Manag. 77 (2014) 690–699.

[20] L. Gao, H. Bai, X. Wu, Numerical analysis of heat transfer in unglazed transpired collectors based on field synergy principle, Sol. Energy 95 (2013) 336–344.

[21] A.A. Pesaran, K.B. Wipke, Use of unglazed transpired solar collectors for desiccant cooling, Pesaran Ahmad A.;Wipke Keith B. 52 (1994).

[22] D. Wang, M. Gao, Q. Gao, Y. Liu, Y. Liu, J. Liu, Experimental and numerical study of the airflow and thermal characteristic of non-uniform transpired solar collector, Build Simul-China 13 (2020) 1305–1319.

[23] D.N. Unglazed, Selective absorber solar air collector: heat exchange analysis, Heat Mass Tran. 36 (2000).

[24] S. Ashish, N.N. Dan, Y. Jc, S. Vicki, J. Phil, A state of art review on the performance of transpired solar collector, Renew. Sustain. Energy Rev. 16 (2012).

[25] V.C. Cristiana, N. Ilinca, I.B. Florin, M. Amina, Thermodynamic investigation on an innovative unglazed transpired solar collector, Sol. Energy (2016) 131.

[26] S. Li, P. Karava, S. Currie, W.E. Lin, E. Savory, Energy modeling of photovoltaic thermal systems with corrugated unglazed transpired solar collectors – Part 1: model development and validation, Sol. Energy 102 (2014) 282–296.

[27] S. Li, P. Karava, Energy modeling of photovoltaic thermal systems with corrugated unglazed transpired solar collectors – Part 2: performance analysis, Sol. Energy 102 (2014) 297–307.

[28] M. Sadegh, An analysis of unglazed transpired solar collectors based on exergetic performance criteria, Int. J. Therm. 13 (2010).

[29] M. G, M. A, M. SS, Experimental study of performance of photovoltaic–thermal unglazed transpired solar collectors (PV/UTCs): energy, exergy, and electrical-to-thermal rational approaches, Sol. Energy 110 (2014).

[30] C. Hoy-Yen, Z. Jie, H.R. Mohd, S. Kamaruzzaman, R. Saffa, Thermal analysis of flat and transpired solar facades, Energy Proc. 48 (2014).

[31] E. Safijahanshahi, M. Salmanzadeh, Performance simulation of combined heat pump with unglazed transpired solar collector, Sol. Energy 180 (2019) 575–593.

[32] M. AL, S. K, Mathematical modeling and thermal performance analysis of unglazed transpired solar collectors, Sol. Energy 81 (2006).

[33] P. Jihong, S. Chao, Y. Shaoxin, Z. Chunxiao, C. Dorota, A. KS, Feasibility investigation on using silver nanorods in energy saving windows for light/heat decoupling, Energy 245 (2022), 123289.

[34] A. Leonardo, A. Karen, F. Adelqui, A. Cristóbal, D.T. Frank, Design and experimental study of a low-cost prefab Trombe wall to improve indoor temperatures in social housing in the Biobío region in Chile, Sol. Energy (2020) 198.

[35] M.R. Hooman, A. Mehran, Energy and exergy study of unglazed transpired collector-2stage, Sol. Energy 132 (2016).

[36] M.R. Collins, H. Abulkhair, An evaluation of heat transfer and effectiveness for unglazed transpired solar air heaters, Sol. Energy 99 (2014) 231–245.

[37] H. Wu, T. Yu, B. Lei, A simplified method for evaluating thermal performances of glazed transpired solar air collector with slit-like perforations, Acta Energiae Solaris Sin. 41 (2020) 246–252.

[38] T.H. Shih, W.W. Liou, A. Shabbir, Z. Yang, Z.J. Zhu, A new k-ε eddy-viscosity model for high Reynolds number turbulent flows - model development and validation, Comput. Fluid 3 (1995) 227–238.

[39] I.B. Celik, U. Ghia, P.J. Roache, C.J. Freitas, H. Coleman, P.E. Raad, Procedure for estimation and reporting of uncertainty due to discretization in CFD applications, J. Fluid Eng. 130 (2008), 78001.

[40] M. Gao, D. Wang, Y. Liu, Y. Wang, Y. Zhou, A study on thermal performance of a novel glazed transpired solar collector with perforating corrugated plate, J. Clean. Prod. 257 (2020), 120443.

[41] S. Farahat, F. Sarhaddi, H. Ajam, Exergetic optimization of flat plate solar collectors, Renew. Energy 34 (2009) 1169–1174.

[42] J.S. Coventry, K. Lovegrove, Development of an approach to compare the 'value' of electrical and thermal output from a domestic PV/thermal system, Sol. Energy 75 (2003) 63–72.

[43] D. Bahrehmand, M. Ameri, M. Gholampour, Energy and exergy analysis of different solar air collector systems with forced convection, Renew. Energy 83 (2015) 1119–1130.

[44] S. Motahar, A.A. Alemrajabi, An analysis of unglazed transpired solar collectors based on exergetic performance criteria, Int. J. Therm. 4 (2010) 153–160.

[45] D. Ibrahim, M.A. Rosen, Exergy: Energy, Environment and Sustainable Development, Newnes, 2012.

[46] H. Gadd, S. Werner, Daily heat load variations in Swedish district heating systems, Appl. Energy 106 (2013) 47–55.